Rotational drift in Antarctic sea ice: pronounced cyclonic features and differences between data products

Wayne de Jager[1], Marcello Vichi[1,2]

[1]Department of Oceanography, University of Cape Town, Cape Town, 7700, South Africa
5   [2]Marine and Antarctic Research Centre for Innovation and Sustainability (MARIS), University of Cape Town, Cape Town, 7700, South Africa

Correspondence to: Wayne de Jager (djgway001@myuct.ac.za)

Abstract. Sea-ice extent variability, a measure based on satellite-derived sea ice concentration measurements, has traditionally been used as an essential climate variable to evaluate the impact of climate change on polar regions. However, concentration-
10   based measurements of ice variability do not allow to discriminate the relative contributions made by thermodynamic and dynamic processes, prompting the need to use sea-ice drift products and develop methods to quantify changes in sea-ice dynamics that would indicate trends in Antarctic ice characteristics. Here, we present a new method to automate the detection of rotational drift features in Antarctic sea ice from space at spatial and temporal scales comparable to that of polar weather. This analysis focusses on drift features in the Atlantic Sector of the Southern Ocean in the period 2013–2020 using currently
15   available satellite ice motion products from EUMETSAT OSI-SAF. We observe a large discrepancy between cyclonic and anticyclonic drift features, with cyclonic features typically exhibiting larger drift intensity and spatial variability according to all products. The mean intensity of the 95th percentile of cyclonic features was 1.5–2.0 times larger for cyclonic features than anticyclonic features. The spatial variability of cyclonic features increased with intensity, indicating that the most intense cyclonic features were also the least homogenous. There was good agreement between products in detecting anticyclonic
20   features, however, larger disagreement was evident for cyclonic features with the merged product showing the most intense 95th percentile threshold and largest spatial variability. A timeseries analysis of the 95th percentile showed an abrupt intensification of cyclonic features from 2014–2017, which coincides with the record decline in Antarctic sea-ice extent since winter of 2015. Our results suggest that this decline is strongly linked to rapidly changing sea-ice dynamics driven by polar storms, and that the variability in the rotational drift of sea ice can be a useful climate index for future studies.

1 Introduction

The Antarctic continent is surrounded by seasonally varying sea ice. During the austral winter, sea-ice coverage expands zonally when progressing northward into the Southern Ocean, and conversely constricts south towards Antarctica's coastline in the austral summer. Sea ice plays a major role in ocean and atmosphere interactions, primarily acting as a heat, mass and momentum exchange modulator between the surface water and overlying air masses (McPhee et al., 1987; Vihma et al., 2014).
30   Sea-ice coverage is a key component of the Southern Ocean climate system and therefore also the global climate system

(Mayewski et al., 2009). Antarctic sea ice is characterized by its high temporal and spatial variability (Parkinson, 2019), and thus it is necessary to define and measure this variability for future trend analysis. Due to the difficulties associated with accessing the polar regions, *in situ* measurements of sea-ice properties are sparse. The detection of sea ice via remote sensing techniques is therefore a critical component of mapping its distribution. Reliable satellite derived sea-ice distribution estimates date back to 1978 (Turner et al., 2016), datasets which are now fundamental to our understanding of sea-ice variability and the backbone of polar climatological analysis.

Traditionally, sea-ice concentration (SIC, a measure of the proportion of ice-covered water to total area) has been derived from the passive microwave (PM) brightness temperature of the ocean surface and used to estimate the sea-ice extent (SIE, a measure of the area of ocean surface covered by 15 % or greater SIC). Trends in SIE are commonly used indicators of sea-ice variability in both the Arctic and Antarctic regions, and subsequently presented to highlight the effects of global warming. Antarctic SIE trends have historically been relatively constant, however, are recently characterized by pronounced variability with regionally distinct trends, with a record high SIE in 2014 declining to a record low SIE in 2017 (Parkinson, 2019; Turner et al., 2017). It is, however, noteworthy that SIE only considers the area of SIC greater than 15 %, and therefore ignores the internal variability within the 15–100 % range. Modelled attempts to simulate the sea-ice extent have shown that uncertainties in this internal variability introduces a far greater bias than that of the satellite retrieval process (Notz, 2014). Furthermore, the decision to define a lower threshold of 15 % in the definition of SIE is one of traditional convention based on the radiometric properties of sea ice relative to that of open water, rather than one based on any dynamic or thermodynamic considerations (Comiso and Zwally, 1984). This highlights a limitation of using the SIE as a metric of ice variability - particularly when attempting to forecast or hindcast sea-ice coverage in models (Notz and Community, 2020). This limitation could potentially be exacerbated in the Southern Ocean. Unlike in the Arctic basin, Antarctic sea ice is unbounded by land, resulting in a far more dispersive and non-uniform growth pattern during the freezing months, and frequent cyclone passages and intense wave induced break up alters the ice landscape far into the ice interior (Kohout et al., 2014; Uotila et al., 2011). Additionally, the weakly stratified upper ocean in the Antarctic results in a considerably higher ocean-to-atmosphere heat flux, thus limiting the growth of sea ice on the ocean surface (Martinson and Iannuzzi, 2013).

While temporal variability in SIC can be computed from PM data, identifying the mechanisms driving this variability is less obvious. Dynamic and thermodynamic processes together alter the Southern Ocean's ice landscape (Stevens and Heil, 2011), however, concentration-only based measurements from space do not allow to discriminate their relative contributions. Ice motion products can therefore be used in conjunction with ice concentration products to help distinguish the dynamical component. These products use a feature-tracking method, whereby a distinguishable pattern in the ice is identified and followed across a temporal sequence of brightness temperature (or backscatter) maps, and the resultant displacement of this pattern over the time interval can then be estimated. This retrieval method, therefore, relies on the persistence of these

distinguishable patterns throughout the time interval. Sea-ice movement is primarily driven by the exchange of momentum

65 from the overlying atmosphere or ocean surface (Biddle and Swart, 2020; Holland and Kwok, 2012). Waves, ocean tilt, Coriolis forcing, ice inertia and internal ice stressors also play a role (Feltham, 2008). Studies using this feature-tracking drift retrieval method have shown that seasonal patterns and long-term trends in Southern Ocean sea-ice drift have a strong correlation with local winds and that ice drift speeds in the period 1992–2010 have increased by up to 30 % (Holland and Kwok, 2012). Satellite derived drift speeds between 1982–2015 were measured to be ~1.4 % of the geostrophic wind, while Arctic drift speeds was

70 approximately half of that over the same period, suggesting that the thinner, weaker and less compact Antarctic sea ice may be more susceptible to wind forcing (Kwok et al., 2017). Furthermore, the El Nino Southern Oscillation (ENSO) and the Southern Annular Mode (SAM) have also been shown to influence sea-ice variability (Goosse et al., 2009; Pezza et al., 2012; Thompson, 2002; Yuan, 2004). However, the degree of relative influence of these larger scale atmospheric modes is debated (Schroeter et al., 2017), and it is becoming increasingly argued that sea-ice variability trends – especially in the Atlantic Sector

75 – are primarily driven by local weather events rather than larger scale atmospheric features (Kwok et al., 2017; Matear et al., 2015). It has been shown that intense polar cyclones can continually reshape the underlying marginal ice zone (MIZ, traditionally defined as the region of sea ice between 15–80 % SIC) and pack ice, as the strong winds induce synoptic scale rotation into the ice floes while carrying warm, moist air along their trajectory (Vichi et al., 2019; Wang et al., 2014). Furthermore, it has been suggested that the unprecedented decrease in SIE between 2014–2016 was partially the result of

80 intense atmospheric storms injecting large scale momentum into the underlying sea ice, causing the ice to drift northward and melt at the warmer lower latitudes (Turner et al., 2017; Wang et al., 2019b). This phenomenon is likely to grow in influence as extratropical cyclones shift poleward and polar storms intensify (Chang, 2017; Tamarin-Brodsky and Kaspi, 2017). It is therefore necessary to consider the effect that local weather systems have on ice dynamics and to evaluate how well the feature-tracking method of drift retrieval performs in conditions of rapidly changing sea-ice properties.

85

This study proposes a method for the detection and quantification of rotational drift features in Antarctic sea ice at temporal and spatial scales similar to that of local weather events. This was done focusing on the Atlantic Sector that is more directly affected by weather variability (Matear et al., 2015), by computing the sea-ice vorticity from satellite ice drift estimates and quantifying the rotational drift of the ice floes within circular domains. This method establishes a measure of rotational drift

90 of sea ice which could be used as a potential climate index with which interannual dynamical trends can be analysed. Several ice motion products are operationally available, all of which undergo shared processing chains but use input data measured by different satellite sensors or remote sensing techniques. While a validation of the vorticity estimates is not included due to the sparsity of *in situ* data, a comparison between the relative performance of four drift products is shown. This study aims to investigate the role of polar weather on driving sea-ice dynamics, and assess to what extent ice drift products are able to capture

95 changes over the period of data availability.

Data

Six different products from the EUMETSAT OSI SAF low resolution sea-ice drift product range (or OSI-405-c) were used in this analysis: the multi-sensor merged, AMSR-2, ASCAT, SSM/I and two SSMIS products. The OSI-405-c processing starts from daily maps of brightness temperature, aggregated from swath data measured from the mentioned sensors, namely: the AMSR-2 on JAXA platform GCOM-W1; the SSM/I on DMSP platform F15, the SSMIS on DMSP platforms F17 and F18 and the backscatter data from the ASCAT sensor on EUMETSAT platform MetOp-A. A Laplacian filter is applied to these daily maps to enhance specific ice features in the image and an ice-edge mask (OSI-402-c product) is also applied. Displacement vectors are then computed from two daily images approximately 48 h apart using a feature-tracking method. The temporal range of these single-sensor products in the Southern Hemisphere are as follows: The AMSR-2 product is available from September 2015 to present; the ASCAT from March 2013 to present; the SSM/I from March 2013 to September 2015; the SSMIS-f17 from September 2015 to April 2018; and the SSMIS-f18 from August 2018 to present. For this analysis, motion vectors derived from the SSMI/S instrument family are grouped to provide a continuous dataset of measurements since 2013. This group will be analysed as a single product and referred to as the SSMI/S product. The multi-sensor merged product implements a two-step process, firstly by using a weighted average of all valid single-sensor data at a particular grid point – where the weighting of each single-sensor product is inversely proportional to the validated error of that product – and secondly by interpolating surrounding vectors for grid points where no data is available from any single-sensor product. The OSI-405-c product range was used because its spatial coverage spans over the entire Antarctic sea ice landscape with a comparably intermediate temporal resolution of approximately 48 h, although the 62.5 km spatial resolution is coarse. The OSI-405-c processing chain uses the Continuous Maximum Cross Correlation method, which includes an additional processing step on the traditionally used Maximum Cross Correlation method. This additional step reduces the high level of quantization noise that typically hinders displacement vector retrieval over short time periods (Lavergne et al., 2010). Vector displacement uncertainties are also included in all OSI-405-c products from 1st June 2017. Antarctic OSI-405-c motion vectors are mapped onto a NSIDC polar stereographic projection (latitude of true scale at 70°S) and are available from April 2013 to present at near real-time – making it a good candidate for year-to-year variability analysis and operational use. Further information on the OSI-405-c product processing chain can be found in Lavergne et al. (2010). Due to the limitations of measuring sea-ice drift in melting conditions and during periods of insufficient ice cover, only the months of June-October were considered, and our analysis focused on the Atlantic Sector of the Southern Ocean, spanning the area between 65° W and 50° E.

3 Methodology

Sea-ice vorticity features were identified using a detection algorithm applied to the single-sensor products (AMSR-2, ASCAT and SSMI/S family) and the merged product. The first step of this process is the computation of the vorticity field for each ≈48 h dataset. Here, using a regularly spaced fixed grid, the vorticity is computed at every square pixel $P_{i,j}$ from the drift vector estimates at $P_{i-1,j}$, $P_{i+1,j}$, $P_{i,j-1}$ and $P_{i,j+1}$:

$$\zeta_{i,j} = \frac{\delta v_{i,j}}{\delta x} - \frac{\delta u_{i,j}}{\delta y} \cong \frac{v_{i+1,j} - v_{i-1,j}}{2\Delta x} - \frac{u_{i,j+1} - u_{i,j-1}}{2\Delta y} \tag{1}$$

where $\zeta_{i,j}$ is the relative vorticity of a pixel $P_{i,j}$ using a centred-in-space scheme, u and v are the zonal and meridional sea-ice velocities respectively, and Δx and Δy is the length and width of a pixel, which in our case is a 62.5 km square. Low-quality flagged drift measurements (i.e., flag values 0-19 in the OSI-405-c product) are rejected, and therefore no vorticity values are computed at those grid points or their adjacent neighbours. Only drift measurements with an acceptable quality flag (i.e., flag values $20-30$) are considered. This range of acceptable flag values was chosen because each drift estimate has a corresponding drift uncertainty (from 1st June 2017), and so while some vectors may be of degraded quality, this potential noise can be quantified and propagated through the vorticity computation.

In the second step of the process, the algorithm generates virtual circular subdomains D_r of radius r centred at every grid point in our vorticity field. Each of these subdomains represent a vorticity feature, which can overlap in space or in time, but never in both. We define the feature intensity as the mean of all vorticity estimates contained within its circumference, and the feature variability as the standard deviation of all vorticity estimates contained within its circumference. Therefore, a negative mean intensity feature represents a circular area of sea ice dominated by cyclonic rotation, while a positive mean intensity feature represents an area dominated by anticyclonic rotation. A minimum pixel validity threshold of T is applied to every subdomain D_r, ensuring that each classified feature has an adequate number of valid vorticity values within its circumference. Subdomains that fail to meet the minimum pixel validity threshold are ignored, thus reducing the algorithm's susceptibility to classifying small regions of intense vorticity at the ice edge or coastline as features. This process is repeated independently per product with varying r (500, 450 and 400 km) and T (90, 85 and 80 %) parameter values, meaning that all identified features contain 180-220 valid vorticity values within their circumference, depending on the choice of r and T. The choice of 500, 450 and 400 km radius features is oriented towards capturing the effect of large-scale synoptic features on the underlying sea ice, which are of the order of 1000 km, and therefore a 62.5 km resolution sea-ice drift product is sufficiently high enough to capture these features. All permutations of varying parameter values radius r and threshold T produced similar results, indicating that the presented results are robust to the choice of free parameters. Results shown in Sect. 4 used $r = 450$ km and $T = 90$ %.

An analysis of the propagation of uncertainties in our feature detection was also done. This follows the methods described in Sect. 2.4 of Dierking et al. (2020). Here, we assume that the position error and uncertainty in the timing of the measurements are negligible, and therefore the uncertainty in vorticity of a square cell in a fixed grid can be estimated by:

$$\sigma_{vort}^2 = \frac{2\sigma_{tr}^2}{L^2 \Delta T^2} \tag{2}$$

where σ_{tr}^2 is the tracking error of the drift vector, L is the length of the square cell, and ΔT is the time interval between two sequential brightness temperature swath measurements. Therefore, all classified vorticity features have an associated uncertainty, which is defined as the mean of all σ_{vort} estimates within the circumference of the feature.

4 Results

4.1 Analysis of uncertainties and comparison of detected features in the drift products

160 Figure 1 shows the distribution of feature intensity relative to its uncertainty for both cyclonic (blue) and anticyclonic (red) features. This analysis was done using years 2017–2020 due to the availability of drift uncertainty estimates in the OSI-405-c product. The intensity of rotational features (~10^{-3} s^{-1}) is approximately 3 orders of magnitude larger than its associated uncertainty (~10^{-6} s^{-1}), mostly due to the large L^2 and ΔT^2 terms in the denominator of Eq. (2). The SSMI/S product showed the largest mean uncertainty for both cyclonic and anticyclonic features, while uncertainties were smallest using the AMSR-2

165 product (Table 1). Despite differences between the three single-sensor products, each of them showed near identical estimates of the mean uncertainty of cyclonic features relative to that of anticyclonic features. Conversely, the merged product showed a larger mean uncertainty for cyclonic features (0.48 ×10^{-6} s^{-1}) than anticyclonic features (0.41 ×10^{-6} s^{-1}), suggesting that cyclonic drift estimates are noisier than that of anticyclonic ones. Single-sensor derived products showed a small range of uncertainties for both cyclonic and anticyclonic features, as indicated by the flatness of scattering in Fig. 1a–f. This is also

170 shown statistically in Table 1, where the standard deviation of the uncertainty spread is approximately 0.04 ×10^{-6} s^{-1} for all three single-sensor products. This is because the tracking error (σ_{tr}^2) term in Eq. (2) is mostly spatially uniform, although there is some variation introduced into the uncertainty field by the poorer quality flagged drift estimates and small deviations in the time interval (ΔT). Conversely, the merged product (Fig. 1g and 1h) showed a far greater standard deviation of uncertainties; 0.15 ×10^{-6} s^{-1} and 0.10 ×10^{-6} s^{-1} for cyclonic and anticyclonic features respectively. This result is intuitive as the merged product

175 is created using a combination of the single-sensor products and its uncertainty is computed as a function of the independent uncertainties of its constituents, and thus the resultant uncertainty of the merged product is expectedly more variable than that of the single-sensor products.
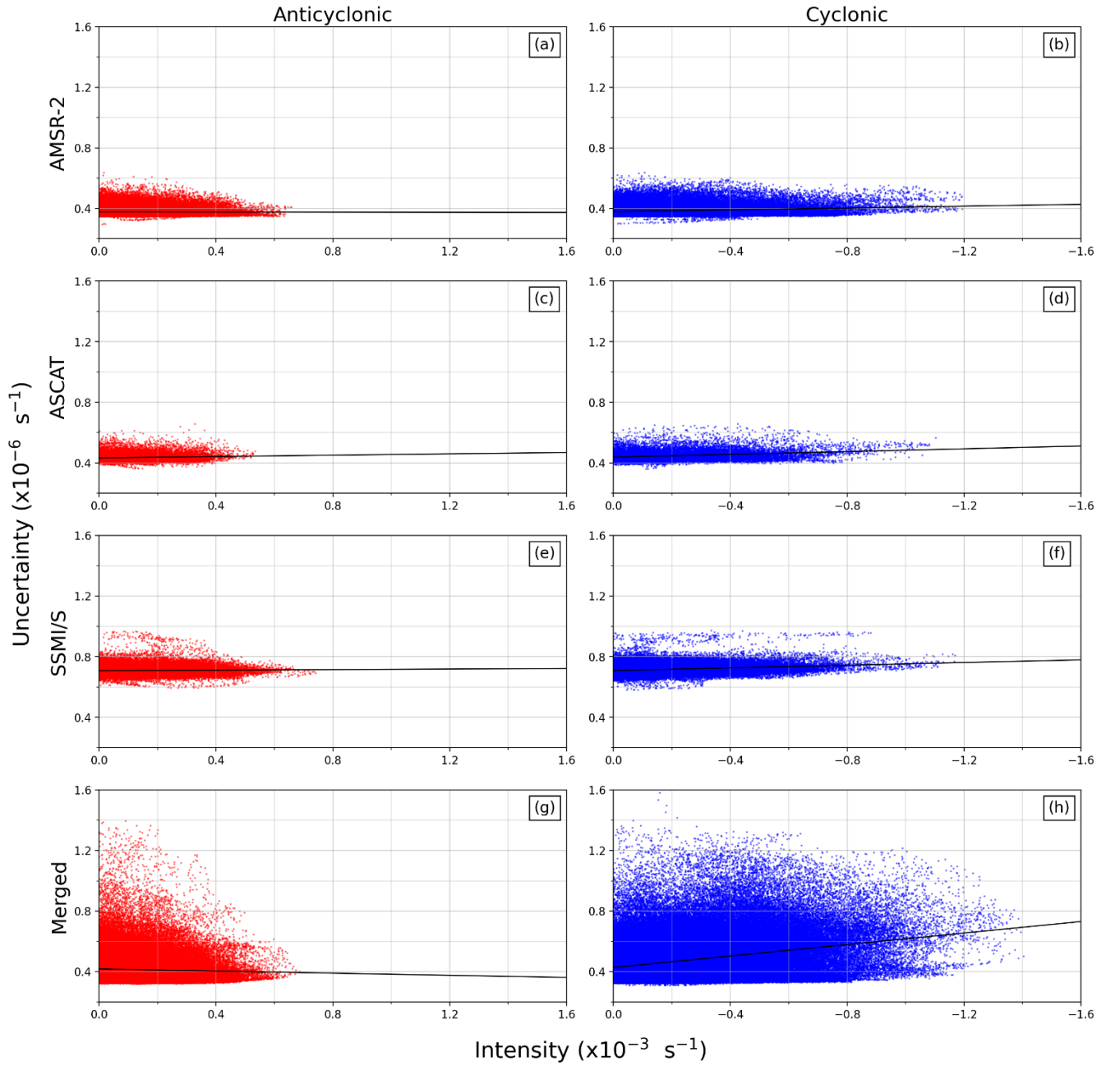
Figure 1: The intensity and uncertainty of vorticity of all features detected between 2017–2020. Cyclonic and anticyclonic features are represented with blue and red dots respectively. Panels (a) and (b) show features detected using the AMSR-2 product; panels (c) and (d) using the ASCAT product; panels (e) and (f) using the SSMI/S product family; and panels (g) and (h) using the merged product. The lines-of-best-fit are shown in black. Note the relative scaling order of magnitude between variables, and the reverted x-axis for cyclonic features to aid comparison.

Table 1: The mean and standard deviation of the uncertainty and variability of vorticity of all features detected between 2017–2020 (Format: Mean ± STD). Note the relative scale of units of the uncertainty estimates relative to that of the variability.

UNCERTAINTY ($\times 10^{-6}\ s^{-1}$)	AMSR-2	ASCAT	SSMI/S	MERGED
Anticyclonic	0.39 ± 0.04	0.44 ± 0.03	0.71 ± 0.03	0.39 ± 0.01
Cyclonic	0.39 ± 0.03	0.45 ± 0.04	0.72 ± 0.04	0.48 ± 0.15
VARIABILITY ($\times 10^{-3}\ s^{-1}$)				
Anticyclonic	0.33 ± 0.11	0.38 ± 0.09	0.38 ± 0.10	0.39 ± 0.17
Cyclonic	0.42 ± 0.14	0.47 ± 0.13	0.46 ± 0.13	0.55 ± 023

190   The relationship between the feature intensity and its associated variability within the search radius (Fig. 2) indicated that they are of the same order of magnitude. Here it can be seen that the scale of standard deviation was far more comparable to the feature intensity. It is shown that the mean variability was larger for cyclonic features than anticyclonic features in all four products, of which the largest spread is noted using the merged product (Table 1). Additionally, all four products agree that the variability of cyclonic features was proportional to its intensity – as visualized by the gradient of the black lines-of-best-fit

195   in Fig. 2b, 2d, 2f, and 2h – indicating that the highest intensity cyclonic features were also the most variable. The merged product had the largest gradient factor of 0.44 for cyclonic features (Fig. 2h), and the single-sensor AMSR-2 (Fig. 2b), ASCAT (Fig. 2d) and SSMI/S (Fig. 2f) products had smaller gradient factors of 0.31, 0.33 and 0.34 respectively. No obvious relationship between intensity and associated variability was seen for anticyclonic features, with the single-sensor AMSR-2 (Fig. 2a), ASCAT (Fig. 2c) and SSMI/S (Fig. 2e) products all showing a gradient factor of approximately 0.01. The merged

200   product had an inversed proportionately gradient factor of -0.10 (Fig. 2g), indicating that intense anticyclonic features are more homogenous.
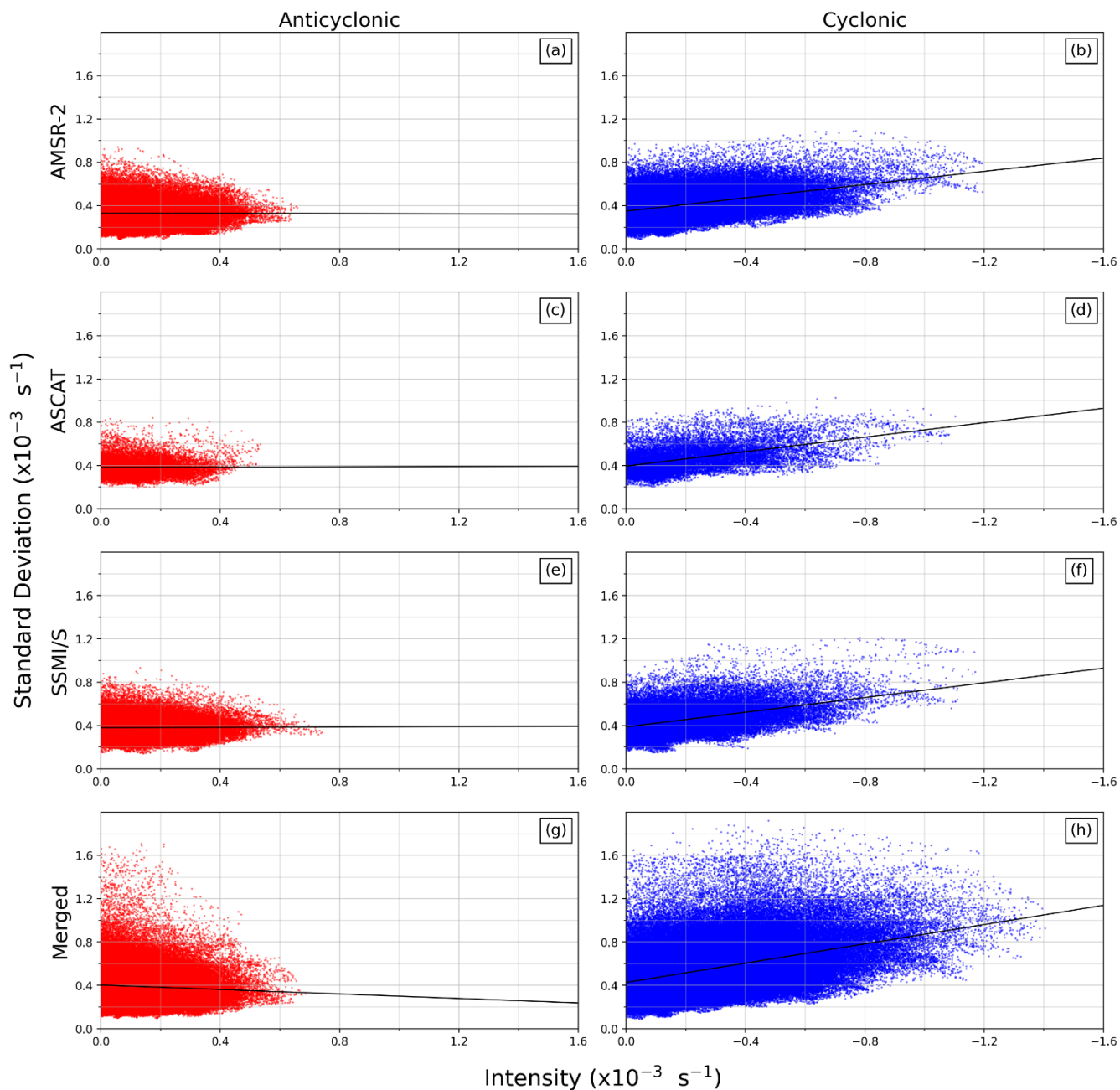
Figure 2: The intensity and standard deviation of vorticity of all features detected between 2017–2020. Cyclonic and anticyclonic features are represented with blue and red dots respectively. Panels (a) and (b) show features detected using the AMSR-2 product; panels (c) and (d) using the ASCAT product; panels (e) and (f) using the SSMI/S product family; and panels (g) and (h) using the merged product. The lines-of-best-fit are shown in black. Note the relative scaling order of magnitude between variables, and the reverted x-axis for cyclonic features to aid comparison. The gradients of the lines-of-best-fit reported in the Results (Sect. 4.1) have been computed using the absolute values of the x-axis to simplify the comparison between the cyclonic and anticyclonic distributions.

205

The disagreement between cyclonic and anticyclonic features is further highlighted in Fig. 3, which shows the intensity
distribution of anticyclonic (Fig. 3a) and cyclonic (Fig. 3b) features. Justified by our vorticity uncertainty analysis between
2017–2020, we have assumed that the negligible importance of this uncertainty can be retroactively applied to earlier years,
and so Fig. 3 is representative of all features detected from 2016-2020 between 1st June to 31st October. We have chosen this
temporal range to maximise the use of available data for which all four products overlap in time. It must be noted that no
SSMI/S ice drift estimates in June and July of 2018 are available, due to the gap in the transition period from the SSMIS-f17
and -f18 platforms. Results show that the intensity of cyclonic features (Fig. 3b) were higher than that of anticyclonic features
(Fig. 3a), as indicated by the heavier tail of the gaussian curve estimate of the cyclonic distribution. A total of 311 758
anticyclonic features were detected over this period, with the most being returned by the merged product (144 491), followed
by the AMSR-2 (84 171), SSMI/S (64 263) and ASCAT (18 383) products. The number of cyclonic features returned was
similar in the single-sensor AMSR-2 (105 889), SSMI/S (66 111) and ASCAT (21 991) products, while the merged product
detected approximately twice as many cyclonic features (295 484) as anticyclonic features. A total of 489 475 cyclonic features
were returned by all four products, 57 % more relative to the total number of anticyclonic features detected. This disagreement
in the number of features detected per product is representative of the quantity of sea-ice drift estimates retrieved, with the
merged product expectedly having the best coverage, followed by the AMSR-2, SSMI/S and ASCAT single-sensor products.

Inter-product comparisons indicate that there is little difference in the intensity of anticyclonic features (Fig. 3a) – as shown
by the similarity of overlapping curve estimates – with only the ASCAT product (blue line) deviating slightly from the other
distributions with a higher frequency of low-intensity features detected (between 0 and -0.2×10^{-3} s^{-1}). Conversely, the cyclonic
distribution curves show a larger discrepancy between products (Fig. 3b), particularly the merged product (yellow line), which
shows a disproportionately small frequency of low-intensity features (between 0 and -0.2×10^{-3} s^{-1}) and high frequency of
intermediate-intensity features (between -0.25×10^{-3} and -0.6×10^{-3} s^{-1}). If the quality flag restriction is relaxed to include all the
available data in the OSI-405-c product datasets, the difference between the distributions is enhanced, with the merged product
showing a much-extended tail of high intensity cyclones (not shown). This indicates that the extent of disagreement between
products is dependent on the choice of quality flags used. Due to the large number of low-intensity features detected, the
differences between products in detecting high-intensity features is less clear. Therefore, the most intense cyclonic and
anticyclonic features for each product were compared. Here, we define the major events as those features above the 95th
percentile (vertical dashed-lines in Fig. 3a and Fig. 3b). Similar thresholds are shown for major anticyclones in the SSMI/S
(0.37×10^{-3} s^{-1}), AMSR-2 (0.36×10^{-3} s^{-1}) and merged (0.35×10^{-3} s^{-1}) products, with the ASCAT (0.32×10^{-3} s^{-1}) product again
deviating slightly from the others (Fig. 3a). For cyclonic features, the merged product (-0.69×10^{-3} s^{-1}) had the most intense
threshold, followed by the AMSR-2 (-0.63×10^{-3} s^{-1}), ASCAT (-0.62×10^{-3} s^{-1}) and SSMI/S (-0.54×10^{-3} s^{-1}) products (Fig. 3b).
The 95th percentile intensity threshold was therefore 1.5–2.0 times larger for cyclonic features than anticyclonic features.

240
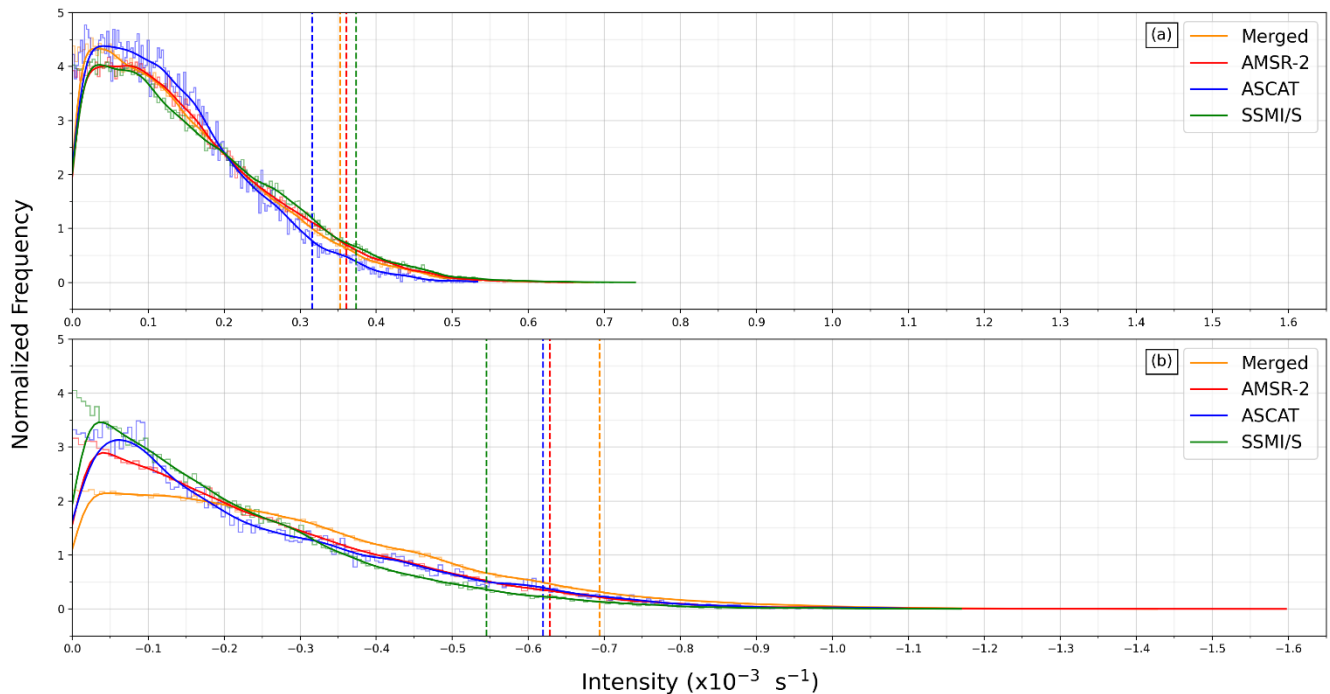
Figure 3: The normalized frequency distribution of (a) anticyclonic vorticity features and (b) cyclonic vorticity features from 2016–2020 (note the reverted x axis for comparison). Lighter shaded lines show a stepped histogram of 200 bins, while the darker shaded curve represents a kernel-density estimate using Gaussian kernels. Vertical dashed lines indicate the intensity threshold of the 95th percentile.

245

4.2 Year-to-year variability

The previous analysis of uncertainties indicated that the difference between the products in the number and intensity of the detected features is robust. A further analysis into the interannual variability of major events was conducted, to assess the presence of year-to-year differences during the period of data availability. The temporal range of analysis was extended to the

250 period 2013–2020, as 2013 is the earliest year of available data in the Southern Hemisphere. However – upon defining the 95th percentile intensity thresholds shown in Fig. 3 – it was noticed that no cyclonic feature exceeded this threshold in 2013 or 2014 for any product. This was also the case at the 90th percentile. It is therefore noteworthy that a strict, consistent intensity threshold applied to all years does not allow us to discern the relative dynamical changes earlier than 2015. For this reason, we have defined the 95th percentile threshold for each year independently. This means that the results presented in Fig. 4 show

255 the interannual intensity distribution of the major cyclonic and anticyclonic features based on each year's distribution. The statistical mean, standard deviation, and intensity threshold of the 95th percentile for each year is also provided to show how different the years are and to justify the choice of this diagnostics (Table 2). Note that the AMSR-2 was only in operational use from September 2015, so no prior data is available, and no SSMI/S ice drift estimates were available in June and July of

2018. There is no obvious interannual trend shown in anticyclonic intensity between 2013–2020 (Fig. 4a, 4c, 4e and 4g),

260   visually indicated by the box-and-whisker rectangles remaining relatively constant in all four products and with few outlier

features detected. This was further supported by the relatively small variability in the mean intensity and standard deviation

between years (Table 2). Conversely, a clear cyclonic interannual trend was evident, characterized by relatively low-intensity

features in 2013 and 2014, followed by an abrupt increase in intensity from 2015–2017 (Fig. 4b, 4d, 4f and 4h). From 2014–

2017, the mean of the 95th percentile of cyclones increased by a factor of 2.8, 2.6 and 1.7 for the ASCAT, SSMI/S and merged

265   products respectively (Table 2). Much like the cyclonic variability-to-intensity relationship described earlier (Fig. 2b, 2d, 2f

and 2h), it was again evident that the standard deviation increases with the intensity from 2014–2017 for each available product

(Table 2). All four products indicated a relatively high frequency of cyclonic outlier features – representing features which

were more intense than the annual upper bound ($> |Q3| + 1.5 \times |IQR|$) – with SSMI/S product showing a larger frequency of

outliers in 2015 (Fig. 4).

270

Table 2: The mean, standard deviation, and intensity threshold of the 95th percentile of all anticyclonic features detected between 2013–2020 (Format: Mean ± STD (Threshold)); Units in $\times 10^{-3}\ s^{-1}$). For comparison, the 95th percentile of all anticyclonic (cyclonic) features from 2016–2020 is 0.36 (0.63) for the AMSR-2; 0.32 (0.62) for the ASCAT; 0.37 (0.54) for the SSMI/S; and 0.35 (0.69) for the merged product as illustrated by the vertical lines in Fig. 3.

ANTICYCLONIC	2013	2014	2015	2016	2017	2018	2019	2020
AMSR-2	-	-	0.43±0.07 (0.37)	0.29±0.04 (0.24)	0.41±0.05 (0.36)	0.36±0.05 (0.31)	0.48±0.06 (0.41)	0.43±0.03 (0.38)
ASCAT	0.33±0.05 (0.29)	0.38±0.05 (0.33)	0.40±0.09 (0.30)	0.28±0.03 (0.25)	0.38±0.03 (0.35)	0.31±0.03 (0.27)	0.39±0.04 (0.34)	0.41±0.05 (0.33)
SSMI/S	0.27±0.04 (0.22)	0.33±0.06 (0.27)	0.45±0.07 (0.37)	0.31±0.05 (0.26)	0.43±0.04 (0.39)	0.34±0.04 (0.30)	0.50±0.06 (0.42)	0.42±0.04 (0.37)
MERGED	0.33±0.05 (0.27)	0.35±0.06 (0.29)	0.43±0.06 (-0.36)	0.35±0.05 (0.29)	0.43±0.06 (0.36)	0.37±0.05 (0.31)	0.46±0.06 (0.38)	0.41±0.03 (0.36)
CYCLONIC								
AMSR-2	-	-	-0.81±0.15 (-0.65)	-0.80±0.18 (-0.63)	-0.82±0.11 (-0.70)	-0.68±0.11 (-0.58	-0.69±0.12 (-0.56)	-0.73±0.11 (-0.61)
ASCAT	-0.29±0.04 (-0.25)	-0.29±0.03 (-0.26)	-0.56±0.07 (-0.45)	-0.76±0.11 (-0.65)	-0.82±0.12 (-0.66)	-0.68±0.09 (-0.57)	-0.72±0.10 (-0.61)	-0.66±0.07 (-0.57)
SSMI/S	-0.39±0.05 (-0.37)	-0.45±0.08 (-0.35)	-0.42±0.11 (-0.34)	-0.58±0.10 (-0.47)	-0.77±0.12 (-0.63)	-0.60±0.10 (-0.49)	-0.66±0.13 (-0.54)	-0.68±0.09 (-0.58)
MERGED	-0.46±0.06 (-0.39)	-0.49±0.06 (-0.41)	-0.76±0.16 (-0.60)	-0.83±0.13 (-0.69)	-0.85±0.10 (-0.72)	-0.83±0.14 (-0.68)	-0.86±0.15 (-0.68)	-0.82±0.11 (-0.69)

275
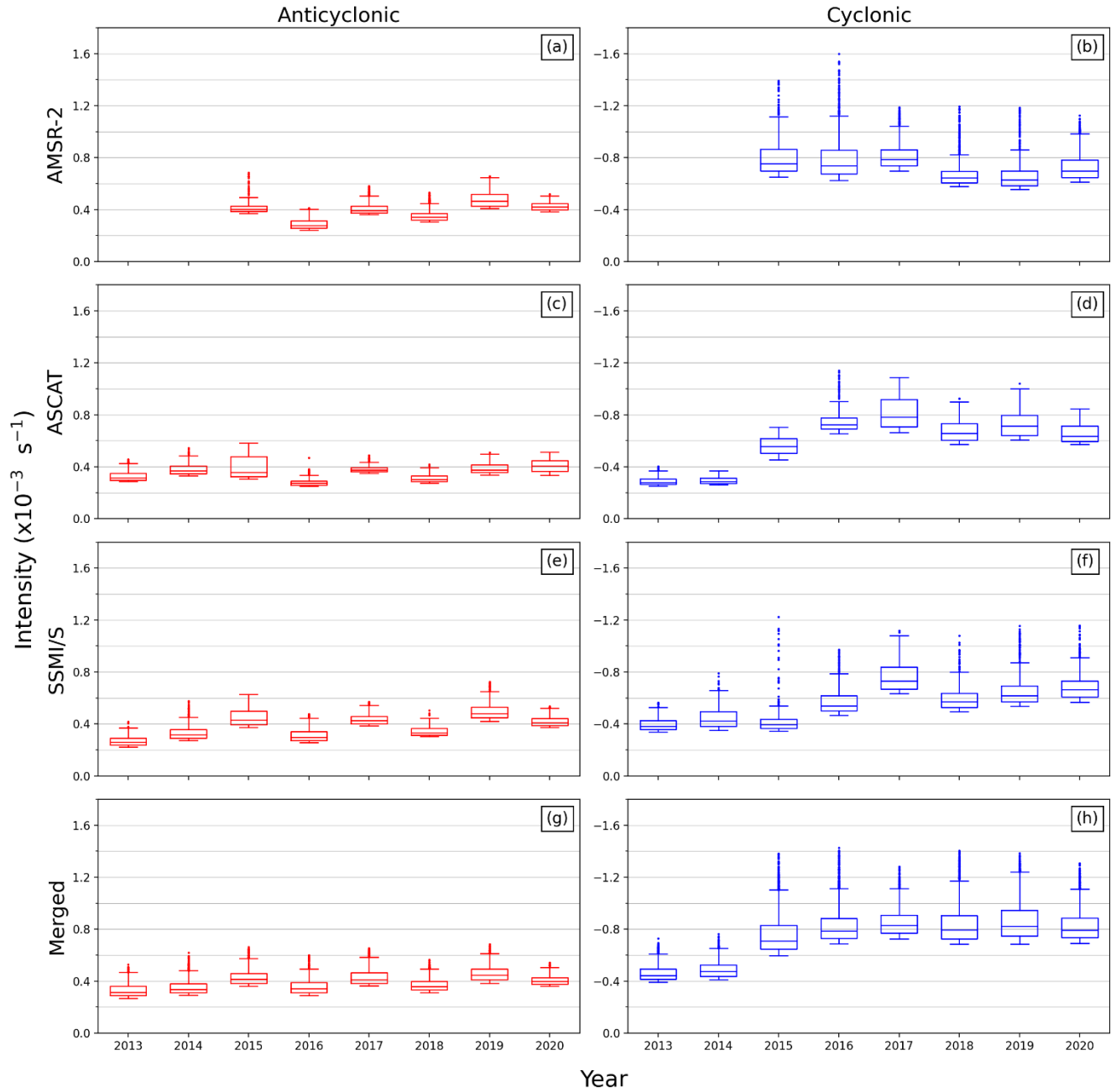
Figure 4: The interannual distribution of the 95th percentile of features detected between 2013–2020. Cyclonic and anticyclonic features are represented with blue and red dots respectively. Panels (a) and (b) show features detected using the AMSR-2 product; panels (c) and (d) using the ASCAT product; panels (e) and (f) using the SSMI/S product family; and panels (g) and (h) using the merged product. The box-and-whisker rectangles indicate the interquartile range (IQR), with the median line separating the upper (Q3) and lower (Q1) quartiles. Outlier features are shown as dots and represent features of which their intensity exceeds the upper bound (> |Q3| + 1.5 × |IQR|) or lower bound (< |Q1| - 1.5 × |IQR|).

5 Discussion and Conclusions

285 This analysis presents a new method to automatically detect and quantify rotational drift in Antarctic sea ice using the EUMETSAT OSI-SAF low resolution sea-ice drift product range. This methodological process has allowed us to establish a measure of rotational drift in Antarctic sea ice at a synoptic scale with the aim to detect current and future changes in sea-ice dynamics from remote sensing. Six products were used in this study, focusing on the Atlantic sector of the Southern Ocean: five single-sensor derived products and one merged product. Rotational features found in the sea ice may originate from both

290 oceanic and atmospheric drivers, and while some initial studies may indicate that sub-mesoscale oceanic processes under the ice may be concurrent drivers (Biddle and Swart, 2020; Stössel et al., 2018), there is larger evidence of the role played by atmospheric cyclones in driving sea-ice motion (Vichi et al, 2019 and references therein). Our analysis is therefore oriented towards capturing these events, assuming that the underlying sea-ice field would be affected at similar spatial scales. For this reason, our detection algorithm identifies circular ice drift features with a radius of 450 km ± 50 km – which is about 6–7 times

295 the spatial resolution of the products and of the scale of atmospheric weather – and quantifies the characteristics of the vorticity field within this circumference.

We observed a large discrepancy in the intensity of detected cyclonic and anticyclonic features and major differences in the intensity distribution of cyclones between the products. This result is robust and significant with respect to the uncertainties in

300 the estimation of the vorticity features as demonstrated in Sect. 4.1. Vorticity is three orders of magnitude greater than its associated uncertainty. However, it was also shown that variability in vorticity within the search radius is of a comparable scale to its intensity (Fig. 2). The high intensity cyclonic features have more variability, while no such relationship is apparent for anticyclonic features. The merged product displayed the largest variability for both cyclonic and anticyclonic features because it combines the drift estimates from the other independent products. The small spread of uncertainty shown by single-

305 sensor products contrasts with their higher spread of spatial variability shown in Fig. 2. This, together with the high signal-to-noise ratio, suggests that the large variability detected is not a symptom of the drift uncertainty. All products detected a higher proportion of intermediate-to-high intensity cyclonic features, as indicated by the heavier tail of the cyclone distribution (Fig. 3a) relative to that of the anticyclones (Fig. 3a). The mean intensity of major cyclonic events was 1.5–2.0 times larger relative to major anticyclonic events between 2016–2020. Inter-product comparisons also show that there was a larger disagreement

310 between products in the distribution of cyclonic features (Fig. 4b) than that of anticyclonic features (Fig. 4a). The merged product had the most intense 95th percentile threshold for cyclonic features and the smallest proportion of low-intensity cyclonic features (Fig. 3b). This is counterintuitive as it is expected that the merged product would show intermediate level results relative to its constituents, like that shown by the merged product in the anticyclonic distribution (Fig. 3a). The merged product also showed the greatest increase in variability relative to cyclonic intensity (Fig. 2b) – illustrated by the steepest

315 gradient of its line-of-best-fit – suggesting that the higher variability detected in the merged product is linked to a larger intensity estimate. Our analysis, however, does not allow us to discern whether the merging process causes an amplification

of cyclonic drift in the sea-ice field, or whether the better coverage of the merged product means it can more accurately detect the rotational drift in the ice compared to the single-sensor products. We hypothesize that the large variability introduced by the merging process is causing an artificial intensification of cyclonic rotation. However, in the absence of independent observation that would corroborate our findings, we are unable to fully identify whether this is an artefact or a feature. Furthermore, the feature-tracking method of drift retrieval may be susceptible to error under conditions of rapid dynamic and thermodynamic changes in sea-ice properties, such as in the event of a strong cyclone traversing the sea ice. It is therefore necessary to consider that rapidly moving ice floes may be blurring the rotational drift we are attempting to estimate over a 48 h period, contributing to the large spatial variability observed in cyclonic features.

The confidence on the method allowed us to perform a provisional analysis of the interannual variations in the most intense cyclonic and anticyclonic features from 2013–2020, although this period is too short to detect any climatic signal. The results show that major anticyclonic events have remained relatively constant from 2013–2020 according to the merged, ASCAT and SSMI/S products. The AMSR-2 detected the same uniformity since its launch in September 2015. Conversely, a substantial change in the interannual distribution of major cyclonic events is evident, where all available products detected an abrupt increase in their intensity from 2014–2017. This increase coincides with the record decline in the Antarctic sea-ice extent observed from late winter 2015 (Parkinson, 2019; Turner et al., 2017). Furthermore, there is also an increase in the number of outlier features per year from 2015 onwards, suggesting that the most intense cyclonic features may have been intensifying further in the last years on record. Among other causes that involve atmospheric and oceanic components (Blanchard-Wrigglesworth et al., 2021; Meehl et al., 2019; Schemm, 2018; Schlosser et al., 2018; Stuecker et al., 2017; Turner et al., 2017; Wang et al., 2019a), it has been argued that an intensification in polar storms in 2016 contributed to the anomalously quickened SIE decline from 2015, as the overlying winds of these synoptic features induced changes in the sea-ice dynamics (Wang et al., 2019b). Our results show that sea ice in the Atlantic sector was more susceptible to cyclonic rotational features after 2015, which can be interpreted as a response to an increased incidence of polar cyclones. If sea ice was thinner and more prone to free-drift motion in general, then we would expect both an increase in cyclonic and anticyclonic rotation. It is known that polar cyclones modify sea ice properties, both through the mechanical forcing of floe drift and the propagation of warm core anomalies over the ice interior (Vichi et al., 2019). Therefore, these modifications may not only have implications on other commonly used ice variability indices, but also on our ability to detect these modifications using currently available remote-sensing data products. While the drift products chosen for this study mostly agree on the detection of anticyclonic features, there is a greater disagreement in detecting cyclonic features. This disagreement has been shown to increase with the inclusion of lower quality data, which implies that it may be an artefact of the sea-ice drift retrieval process. Prior to performing further analysis of drift variability and longer-term trends linked to polar atmosphere variability, further validation of the vorticity metric with *in situ* experiments is required to better discern the differences between products. A better understanding of these features is required before the rotational drift of sea ice can be confidently used as an essential climate variable.

Acknowledgements

350

This work has received funding from the National Research Foundation of South Africa (South African National Antarctic Programme, Project No. 118745).

We would like to acknowledge and give thanks to our reviewers, Dr Thomas Lavergne and Dr Valentin Ludwig, for their time invested into our work. Your comments and suggestions have helped us to improve the quality of our paper and to expand

355 beyond the initial brief communication; your efforts are greatly appreciated. Furthermore, thank you to our handling editor, Dr Christian Haas.

Data availability

The OSI-405-c product FTP server is available at ftp://osisaf.met.no/archive/ice/drift_lr/. The python script to compute and

360 extract the cyclonic and anticyclonic features from the OSI-405-c 48 h datasets is available at: https://github.com/waynedejagerUCT/cryosphere/blob/276a1909eff9e3ae2490bebd6a0e08ca8a707827/VorticityFeatureDetection_v001

References

Biddle, L. C. and Swart, S.: The Observed Seasonal Cycle of Submesoscale Processes in the Antarctic Marginal Ice Zone, J. Geophys. Res. Ocean., doi:10.1029/2019JC015587, 2020.

365 Blanchard-Wrigglesworth, E., Roach, L. A., Donohoe, A. and Ding, Q.: Impact of Winds and Southern Ocean SSTs on Antarctic Sea Ice Trends and Variability, J. Clim., 34(3), 949–965, doi:10.1175/JCLI-D-20-0386.1, 2021.

Chang, E. K. M.: Projected Significant Increase in the Number of Extreme Extratropical Cyclones in the Southern Hemisphere, J. Clim., 30(13), 4915–4935, doi:10.1175/JCLI-D-16-0553.1, 2017.

Comiso, J. C. and Zwally, H. J.: Concentration gradients and growth/decay characteristics of the seasonal sea ice cover., J.

370 Geophys. Res., doi:10.1029/JC089iC05p08081, 1984.

Feltham, D. L.: Sea Ice Rheology, Annu. Rev. Fluid Mech., 40(1), 91–112, doi:10.1146/annurev.fluid.40.111406.102151, 2008.

Goosse, H., Lefebvre, W., de Montety, A., Crespin, E. and Orsi, A. H.: Consistent past half-century trends in the atmosphere, the sea ice and the ocean at high southern latitudes, Clim. Dyn., 33(7–8), 999–1016, doi:10.1007/s00382-008-0500-9, 2009.

375 Holland, P. R. and Kwok, R.: Wind-driven trends in Antarctic sea-ice drift, Nat. Geosci., 5(12), 872–875, doi:10.1038/ngeo1627, 2012.

Kohout, A. L., Williams, M. J. M., Dean, S. M. and Meylan, M. H.: Storm-induced sea-ice breakup and the implications for ice extent, Nature, doi:10.1038/nature13262, 2014.

380 Kwok, R., Pang, S. S. and Kacimi, S.: Sea ice drift in the Southern Ocean: Regional patterns, variability, and trends, edited by J. W. Deming and E. C. Carmack, Elem. Sci. Anthr., 5, doi:10.1525/elementa.226, 2017.

Lavergne, T., Eastwood, S., Teffah, Z., Schyberg, H. and Breivik, L.-A.: Sea ice motion from low-resolution satellite sensors: An alternative method and its validation in the Arctic, J. Geophys. Res., 115(C10), C10032, doi:10.1029/2009JC005958, 2010.

Martinson, D. G. and Iannuzzi, R. A.: Antarctic Ocean-Ice Interaction: Implications from Ocean Bulk Property Distributions in the Weddell Gyre., 2013.

385 Matear, R. J., O'Kane, T. J., Risbey, J. S. and Chamberlain, M.: Sources of heterogeneous variability and trends in Antarctic sea-ice, Nat. Commun., 6(1), 8656, doi:10.1038/ncomms9656, 2015.

Mayewski, P. A., Meredith, M. P., Summerhayes, C. P., Turner, J., Worby, A., Barrett, P. J., Casassa, G., Bertler, N. A. N., Bracegirdle, T., Naveira Garabato, A. C., Bromwich, D., Campbell, H., Hamilton, G. S., Lyons, W. B., Maasch, K. A., Aoki, S., Xiao, C. and van Ommen, T.: State of the Antarctic and Southern Ocean climate system, Rev. Geophys., 47(1), RG1003, 390 doi:10.1029/2007RG000231, 2009.

McPhee, M. G., Maykut, G. A. and Morison, J. H.: Dynamics and thermodynamics of the ice/upper ocean system in the marginal ice zone of the Greenland Sea, J. Geophys. Res., 92(C7), 7017, doi:10.1029/JC092iC07p07017, 1987.

Meehl, G. A., Arblaster, J. M., Chung, C. T. Y., Holland, M. M., DuVivier, A., Thompson, L., Yang, D. and Bitz, C. M.: Sustained ocean changes contributed to sudden Antarctic sea ice retreat in late 2016, Nat. Commun., 10(1), 14, 395 doi:10.1038/s41467-018-07865-9, 2019.

Notz, D.: Sea-ice extent and its trend provide limited metrics of model performance, Cryosphere, doi:10.5194/tc-8-229-2014, 2014.

Notz, D. and Community, S.: Arctic Sea Ice in CMIP6, Geophys. Res. Lett., 47(10), doi:10.1029/2019GL086749, 2020.

Parkinson, C. L.: A 40-y record reveals gradual Antarctic sea ice increases followed by decreases at rates far exceeding the 400 rates seen in the Arctic, Proc. Natl. Acad. Sci., 116(29), 14414–14423, doi:10.1073/pnas.1906556116, 2019.

Pezza, A. B., Rashid, H. A. and Simmonds, I.: Climate links and recent extremes in antarctic sea ice, high-latitude cyclones, Southern Annular Mode and ENSO, Clim. Dyn., 38(1–2), 57–73, doi:10.1007/s00382-011-1044-y, 2012.

Schemm, S.: Regional Trends in Weather Systems Help Explain Antarctic Sea Ice Trends, Geophys. Res. Lett., 45(14), 7165–7175, doi:10.1029/2018GL079109, 2018.

405 Schlosser, E., Haumann, F. A. and Raphael, M. N.: Atmospheric influences on the anomalous 2016 Antarctic sea ice decay, Cryosph., 12(3), 1103–1119, doi:10.5194/tc-12-1103-2018, 2018.

Schroeter, S., Hobbs, W. and Bindoff, N. L.: Interactions between Antarctic sea ice and large-scale atmospheric modes in CMIP5 models, Cryosph., 11(2), 789–803, doi:10.5194/tc-11-789-2017, 2017.

Stevens, R. P. and Heil, P.: The interplay of dynamic and thermodynamic processes in driving the ice-edge location in the 410 Southern Ocean, Ann. Glaciol., 52(57), 27–34, doi:10.3189/172756411795931642, 2011.

Stössel, A., von Storch, J.-S., Notz, D., Haak, H. and Gerdes, R.: High-frequency and meso-scale winter sea-ice variability in the Southern Ocean in a high-resolution global ocean model, Ocean Dyn., 68(3), 347–361, doi:10.1007/s10236-018-1135-y, 2018.

Stuecker, M. F., Bitz, C. M. and Armour, K. C.: Conditions leading to the unprecedented low Antarctic sea ice extent during 415 the 2016 austral spring season, Geophys. Res. Lett., 44(17), 9008–9019, doi:10.1002/2017GL074691, 2017.

Tamarin-Brodsky, T. and Kaspi, Y.: Enhanced poleward propagation of storms under climate change, Nat. Geosci., 10(12), 908–913, doi:10.1038/s41561-017-0001-8, 2017.

Thompson, D. W. J.: Interpretation of Recent Southern Hemisphere Climate Change, Science (80-.)., 296(5569), 895–899, doi:10.1126/science.1069270, 2002.

420 Turner, J., Scott Hosking, J., Marshall, G. J., Phillips, T. and Bracegirdle, T. J.: Antarctic sea ice increase consistent with intrinsic variability of the Amundsen sea low, Clim. Dyn., doi:10.1007/s00382-015-2708-9, 2016.

Turner, J., Phillips, T., Marshall, G. J., Hosking, J. S., Pope, J. O., Bracegirdle, T. J. and Deb, P.: Unprecedented springtime retreat of Antarctic sea ice in 2016, Geophys. Res. Lett., doi:10.1002/2017GL073656, 2017.

Uotila, P., Vihma, T., Pezza, A. B., Simmonds, I., Keay, K. and Lynch, A. H.: Relationships between Antarctic cyclones and 425 surface conditions as derived from high-resolution numerical weather prediction data, J. Geophys. Res. Atmos., doi:10.1029/2010JD015358, 2011.

Vichi, M., Eayrs, C., Alberello, A., Bekker, A., Bennetts, L., Holland, D., Jong, E., Joubert, W., MacHutchon, K., Messori, G., Mojica, J. F., Onorato, M., Saunders, C., Skatulla, S. and Toffoli, A.: Effects of an Explosive Polar Cyclone Crossing the

Antarctic Marginal Ice Zone, Geophys. Res. Lett., 46(11), 5948–5958, doi:10.1029/2019GL082457, 2019.

430   Vihma, T., Pirazzini, R., Fer, I., Renfrew, I. A., Sedlar, J., Tjernström, M., Lüpkes, C., Nygård, T., Notz, D., Weiss, J., Marsan, D., Cheng, B., Birnbaum, G., Gerland, S., Chechin, D. and Gascard, J. C.: Advances in understanding and parameterization of small-scale physical processes in the marine Arctic climate system: a review, Atmos. Chem. Phys., 14(17), 9403–9450, doi:10.5194/acp-14-9403-2014, 2014.

Wang, G., Hendon, H. H., Arblaster, J. M., Lim, E.-P., Abhik, S. and van Rensch, P.: Compounding tropical and stratospheric
435   forcing of the record low Antarctic sea-ice in 2016, Nat. Commun., 10(1), 13, doi:10.1038/s41467-018-07689-7, 2019a.

Wang, Z., Turner, J., Sun, B., Li, B. and Liu, C.: Cyclone-induced rapid creation of extreme Antarctic sea ice conditions, Sci. Rep., doi:10.1038/srep05317, 2014.

Wang, Z., Turner, J., Wu, Y. and Liu, C.: Rapid decline of total Antarctic sea ice extent during 2014–16 controlled by wind-driven sea ice drift, J. Clim., doi:10.1175/JCLI-D-18-0635.1, 2019b.

440   Yuan, X.: ENSO-related impacts on Antarctic sea ice: A synthesis of phenomenon and mechanisms, Antarct. Sci., doi:10.1017/S0954102004002238, 2004.